


RESEARCH

Open Access



BiVO₄/Fe₃O₄@polydopamine superparticles for tumor multimodal imaging and synergistic therapy

Ze Wang^{1†}, Guan Wang^{4†}, Tingting Kang^{1†}, Shuwei Liu¹, Lu Wang⁵, Haoyang Zou^{2*}, Yu Chong^{3*} and Yi Liu^{1*} 

Abstract

Background: Despite tremendous progress has been achieved in tumor theranostic over the past decade, accurate identification and complete eradication of tumor cells remain a great challenge owing to the limitation of single imaging modality and therapeutic strategy.

Results: Herein, we successfully design and construct BiVO₄/Fe₃O₄@polydopamine (PDA) superparticles (SPs) for computed tomography (CT)/photoacoustic (PA)/magnetic resonance (MR) multimodal imaging and radiotherapy (RT)/photothermal therapy (PTT) synergistic therapy toward oral epithelial carcinoma. On the one hand, BiVO₄ NPs endow BiVO₄/Fe₃O₄@PDA SPs with impressive X-ray absorption capability due to the high X-ray attenuation coefficient of Bi, which is beneficial for their utilization as radiosensitizers for CT imaging and RT. On the other hand, Fe₃O₄ NPs impart BiVO₄/Fe₃O₄@PDA SPs with the superparamagnetic property as a T₂-weighted contrast agent for MR imaging. Importantly, the aggregation of Fe₃O₄ NPs in SPs and the presence of PDA shell greatly improve the photothermal conversion capability of SPs, making BiVO₄/Fe₃O₄@PDA SPs as an ideal photothermal transducer for PA imaging and PTT. By integrating advantages of various imaging modalities (CT/PA/MR) and therapeutic strategies (RT/PTT), our BiVO₄/Fe₃O₄@PDA SPs exhibit the sensitive multimodal imaging feature and superior synergistic therapeutic efficacy on tumors.

Conclusions: Since there are many kinds of building blocks with unique properties appropriating for self-assembly, our work may largely enrich the library of nanomaterials for tumor diagnosis and treatment.

Keywords: Fe₃O₄ nanoparticles, BiVO₄ nanoparticles, Superparticles, Multimodal imaging, Synergy therapy

Background

Radiotherapy (RT) is one of the most widely used clinical strategies for cancer treatment [1–4]. More than 50% of cancer patients suffering from solid tumors are under

treatment of RT [5]. Benefiting from the high intensity ionizing radiations (such as electrons, protons, and photons), RT can directly introduce deoxyribonucleic acid (DNA) double-strand breaks or yield a large number of cytotoxic reactive oxygen species (ROS) to trigger the apoptosis or necrosis of irradiated cancer cells [6–9]. However, the therapeutic efficacy of conventional RT is still limited by the insufficient radiation energy deposition on tumor tissues, as well as the serious toxic effects on normal surrounding healthy tissues [10, 11]. Along with the development of nanotechnology and materials science, nanomaterials containing high-Z elements are exploited as radiosensitizers due to their high radiation energy deposition, thereby amplify the radiation-induced

*Correspondence: zzhyy2004@126.com; chongyu@suda.edu.cn;

yiliu@chem.jlu.edu.cn

[†]Ze Wang, Guan Wang and Tingting Kang contributed equally to this work

¹ State Key Laboratory of Supramolecular Structure and Materials, Jilin University, Changchun 130012, People's Republic of China

² Key Laboratory of Polymer Ecomaterials, Changchun Institute of Applied Chemistry, Chinese Academy of Sciences, Changchun 130012, People's Republic of China

³ State Key Laboratory of Radiation Medicine and Protection, School for Radiological and Interdisciplinary Sciences (RAD-X), Collaborative Innovation Center of Radiation Medicine of Jiangsu Higher Education Institutions, Soochow University, Suzhou 215123, People's Republic of China

Full list of author information is available at the end of the article



© The Author(s) 2021. This article is licensed under a Creative Commons Attribution 4.0 International License, which permits use, sharing, adaptation, distribution and reproduction in any medium or format, as long as you give appropriate credit to the original author(s) and the source, provide a link to the Creative Commons licence, and indicate if changes were made. The images or other third party material in this article are included in the article's Creative Commons licence, unless indicated otherwise in a credit line to the material. If material is not included in the article's Creative Commons licence and your intended use is not permitted by statutory regulation or exceeds the permitted use, you will need to obtain permission directly from the copyright holder. To view a copy of this licence, visit <http://creativecommons.org/licenses/by/4.0/>. The Creative Commons Public Domain Dedication waiver (<http://creativecommons.org/publicdomain/zero/1.0/>) applies to the data made available in this article, unless otherwise stated in a credit line to the data.

damage on tumor tissues, accompanied by the alleviation of the relevant side effects [12–15]. On the other hand, deriving from the abnormal blood vasculature, hypoxia is considered as the hostile feature of the tumor micro-environment (TME) to cause irreversible tumor metastasis and RT resistance [16–18]. As a novel therapeutic approach, photothermal therapy (PTT) is an efficient way to overcome this problem [19–21]. Under NIR light irradiation, photothermal agents not only generate regional hyperthermia to ablate cancer cells, but also promote the blood flow and oxygen pressure levels in tumor tissues, resulting in enhancing the tumor cell sensitivity to RT. Therefore, it is reasonable to believe that a superior synergistic therapeutic efficacy from RT and PTT will be achieved by taking advantages of radiosensitizers and photothermal agents simultaneously.

It is well known that imaging techniques play the pivotal role in clinical diagnosis and efficacy evaluation [22]. Although various imaging techniques have been rapidly developed for many years, information collected by a single imaging modality is usually limited and insufficient due to the intrinsic restrictions of each modality [23]. For example, computed tomography (CT) imaging is good at constructing 3D visualization with anatomical details, but suffering from the low resolution [24]. Magnetic resonance (MR) imaging can scan objects with high resolution, but at the expense of the time-consuming data acquisition process [25]. Photoacoustic (PA) imaging is capable of providing the fast real-time monitor and unveils information with high signal-to-noise ratio, but only appropriate to soft tissues [26]. Hence, integrating different imaging modalities into a single nanostructure may hold great potentials to achieve complementary information for tumor diagnosis precisely, accurately and efficiently. Because of the high X-ray absorption coefficient ($5.74 \text{ cm}^2 \text{ g}^{-1}$ at 100 keV) and low cytotoxicity, bismuth (Bi)-based nanomaterials can be seen as an ideal radiosensitizer for CT imaging and RT [27]. Since most of previous Bi-based radiosensitizers focus on Bi_2S_3 and BiOX ($X = \text{Cl}, \text{Br}, \text{I}$), other Bi-based nanomaterials are still needed to be explored to enrich their candidates [28, 29]. In addition, due to the excellent superparamagnetic, Fe_3O_4 NPs have been approved by FDA for T_2 -weighted MR imaging [30]. Most recently, it is reported that Fe_3O_4 NP aggregates exhibit an enhanced photothermal conversion capability comparing to their individual NPs owing to the collective effect [31]. The as-prepared Fe_3O_4 NP aggregates are also verified to have the potential to be used as the photothermal agents for PA imaging and PTT. Thus, constructing nanostructures containing Bi-based nanomaterials and Fe_3O_4 NPs is of great significance in realizing the multimodal imaging and synergistic therapy.

Self-assembly, which mainly depend on the supra-molecular interactions (including van der Waals (vdW) interaction, electrostatic interaction, dipole interaction, hydrogen bonding, hydrophobic interaction and π - π stacking interaction) between building blocks, has been widely used to construct assemblies with different morphologies and formations [32]. During self-assembly, the intrinsic physical and chemical properties of the building blocks are usually passed to the resulting assemblies entirely, which offer us a simple and flexible method to construct nanostructures with desired compositions and functions [33]. Herein, we successfully design and prepare $\text{BiVO}_4/\text{Fe}_3\text{O}_4$ @polydopamine (PDA) superparticles (SPs) for CT/PA/MR multimodal imaging and RT/PTT synergistic therapy. BiVO_4 and Fe_3O_4 NPs with the average sizes of 7.12 and 5.49 nm are firstly prepared, followed by their subsequent self-assembly into $\text{BiVO}_4/\text{Fe}_3\text{O}_4$ SPs via the oil-in-water microemulsion route. After that, the as-prepared $\text{BiVO}_4/\text{Fe}_3\text{O}_4$ SPs are covered by PDA to further improve their photothermal conversion capability. At last, the imaging and therapy performances of $\text{BiVO}_4/\text{Fe}_3\text{O}_4$ @PDA SPs are evaluated via in vitro and in vivo experiments. The results clearly manifest that our $\text{BiVO}_4/\text{Fe}_3\text{O}_4$ @PDA SPs can be seen as the potential nanomedicine for tumor theranostic.

Results and discussion

$\text{BiVO}_4/\text{Fe}_3\text{O}_4$ @PDA SPs are constructed upon the self-assembly of BiVO_4 and Fe_3O_4 NPs following by coating with the PDA shell. Typically, BiVO_4 NPs are prepared through our previous two-phase method, and Fe_3O_4 NPs are prepared via the classical thermal decomposition method [34, 35]. Transmission electron microscopy (TEM) images in Fig. 1a and b show that both of BiVO_4 and Fe_3O_4 NPs are monodispersed nanospheres with the average diameters around 7.12 and 5.49 nm, respectively. High-resolution TEM (HRTEM) images exhibit the lattice fringes with the interplanar spacings of 0.312 and 0.244 nm, corresponding to the (112) planes of monoclinic BiVO_4 and the (311) planes of cubic Fe_3O_4 . X-ray diffraction (XRD) patterns of BiVO_4 and Fe_3O_4 NPs further identify the monoclinic crystal structure of BiVO_4 NPs and the cubic crystal structure of Fe_3O_4 NPs (Additional file 1: Figure S1).

Then, oil-in-water microemulsion method is employed to construct $\text{BiVO}_4/\text{Fe}_3\text{O}_4$ SPs using BiVO_4 and Fe_3O_4 NPs as the building blocks while sodium dodecyl sulfate (SDS) as the surfactants [36]. The as-prepared SDS-capped $\text{BiVO}_4/\text{Fe}_3\text{O}_4$ SPs are nanospheres with the average diameter of 81.20 nm (Fig. 1c). The element distributions of $\text{BiVO}_4/\text{Fe}_3\text{O}_4$ SPs are characterized by energy-dispersive X-ray spectroscopy (EDS) elemental mapping (Additional file 1: Figure S2). Bi, V and Fe are

uniformly distributed throughout the entire SPs, further demonstrating the assembled configuration of the as-prepared $\text{BiVO}_4/\text{Fe}_3\text{O}_4$ SPs. Benefiting from the flexibility of the self-assembly technique, the size and composition of $\text{BiVO}_4/\text{Fe}_3\text{O}_4$ SPs is tunable deliberately. For example, by increasing the toluene-to-water ratio from 1:5 to 2:5, the size of $\text{BiVO}_4/\text{Fe}_3\text{O}_4$ SPs can be increased from 81.20 to 164.50 nm (Additional file 1: Figure S3). In the meantime, upon adjusting the feeding ratio between BiVO_4 and Fe_3O_4 NPs during self-assembly, the molar ratio of Bi/Fe in the as-prepared $\text{BiVO}_4/\text{Fe}_3\text{O}_4$ SPs is varied from 3.5:1 to 1.2:1. The corresponding products are designated as $\text{BiVO}_4/\text{Fe}_3\text{O}_4$ -1, $\text{BiVO}_4/\text{Fe}_3\text{O}_4$ -2 and $\text{BiVO}_4/\text{Fe}_3\text{O}_4$ -3 SPs (Additional file 1: Table S1).

At last, dopamine (DA) monomers are oxidized followed by spontaneous polymerization on the surface of $\text{BiVO}_4/\text{Fe}_3\text{O}_4$ SPs under the alkaline condition [37]. The thickness of the PDA shell is positively correlated with the amount of DA, which will be increased from 10.00 to 80.00 nm when the concentration of DA increases from 0.3 to 0.8 mg/mL (Additional file 1: Figure S4). Given that nanomaterials larger than 120.00 nm can hardly enter into cells upon cellular phagocytosis, $\text{BiVO}_4/\text{Fe}_3\text{O}_4$ SPs with the diameter around 80.00 nm is selected as the core and the PDA shell thickness is designed to be around 10.00 nm.

Since the aggregation of Fe_3O_4 NPs and the presence of the PDA shell can remarkably increase the molar extinction coefficient of monodispersed Fe_3O_4 NPs (Additional file 1: Figure S5), leading to the enhancement in their photothermal conversion capability, the photothermal conversion capability of $\text{BiVO}_4/\text{Fe}_3\text{O}_4$ @PDA SPs suspension is evaluated under 808 nm irradiation. As shown in Fig. 2a, the photothermal conversion capability of $\text{BiVO}_4/\text{Fe}_3\text{O}_4$ @PDA SPs is enhanced by elevating the proportion of Fe_3O_4 in SPs. At the same time, the temperature of $\text{BiVO}_4/\text{Fe}_3\text{O}_4$ @PDA SPs aqueous solution rises rapidly by increasing the power density of the applied laser and the concentration of SPs (Fig. 2b and c). Under 1 W/cm² irradiation for 10 min, the aqueous solution containing 200 µg/mL of $\text{BiVO}_4/\text{Fe}_3\text{O}_4$ @PDA SPs exhibits a noticeable temperature increment of 25 °C. Based on the reported model, the photothermal conversion efficiency of as-prepared $\text{BiVO}_4/\text{Fe}_3\text{O}_4$ @PDA SPs is estimated to be 33.42%, which is comparable to previous reports (Additional file 1: Figure S6) [31]. To balance the properties deriving from BiVO_4 and Fe_3O_4 , $\text{BiVO}_4/\text{Fe}_3\text{O}_4$ @PDA SPs with the Bi/Fe element ratio of 1.8/1 are selected for the following in vitro and in vivo experiments.

Prior to assessing the imaging performance of $\text{BiVO}_4/\text{Fe}_3\text{O}_4$ @PDA SPs, their cytotoxicity is evaluated via standard Cell Counting Kit 8 (CCK-8) assay. After incubation

with $\text{BiVO}_4/\text{Fe}_3\text{O}_4$ @PDA SPs at different concentrations for 24 h, the cell viability of oral epithelial carcinoma (KB) cells is higher than 80% even at a high concentration of 300 µg/mL, which strongly manifest the negligible cytotoxicity of $\text{BiVO}_4/\text{Fe}_3\text{O}_4$ @PDA SPs (Additional file 1: Figure S7). The colloidal stability of $\text{BiVO}_4/\text{Fe}_3\text{O}_4$ @PDA SPs is tested as well. After storage in water, saline, cell culture or serum-containing cell culture for 24 h, $\text{BiVO}_4/\text{Fe}_3\text{O}_4$ @PDA SPs are well dispersed without any visible coagulation (Additional file 1: Figure S8). The low toxicity plus the high colloidal stability provide a powerful guarantee for the utilization of $\text{BiVO}_4/\text{Fe}_3\text{O}_4$ @PDA SPs in tumor theranostic.

Subsequently, the in vitro imaging performances of $\text{BiVO}_4/\text{Fe}_3\text{O}_4$ @PDA SPs are exhibited in Fig. 3a–c. Owing to the high X-ray attenuation coefficient of Bi, the CT signal intensities of $\text{BiVO}_4/\text{Fe}_3\text{O}_4$ @PDA SPs increase linearly and sharply with their concentrations. The Hounsfield units (HU) value of $\text{BiVO}_4/\text{Fe}_3\text{O}_4$ @PDA SPs is calculated to be 28.2136 HU mL mg⁻¹, which is comparable to the clinically used CT contrast agent iobitridol (25.6570 HU mL mg⁻¹) (Fig. 3a). Further increasing the proportion of BiVO_4 in SPs can improve the CT imaging performance of $\text{BiVO}_4/\text{Fe}_3\text{O}_4$ @PDA SPs undoubtedly, but may lose their PA and MR imaging performances as the price. In addition, $\text{BiVO}_4/\text{Fe}_3\text{O}_4$ @PDA SPs are also anticipated to be the MR imaging contrast agents owing to the superparamagnetic property of Fe_3O_4 NPs. Their MR imaging contrast is enhanced in a concentration-dependent manner, and the r_2 value is estimated to be 186 mM⁻¹ s⁻¹, which is higher than current commercial MR contrasts, such as Resovist (143 mM⁻¹ s⁻¹) and Feridex (93 mM⁻¹ s⁻¹) (Fig. 3b). Furthermore, benefiting from the excellent photothermal conversion capability, there is a good linear relationship between the concentration of $\text{BiVO}_4/\text{Fe}_3\text{O}_4$ @PDA SPs and their PA signal under NIR irradiation, suggesting their great potentials as the PA contrast agents (Fig. 3c). Then, in order to prove the concept that our $\text{BiVO}_4/\text{Fe}_3\text{O}_4$ @PDA SPs have the potential to be used for imaging in vivo, multimode CT/MR/PA imaging properties of $\text{BiVO}_4/\text{Fe}_3\text{O}_4$ @PDA SPs are explored on the subcutaneous tumor model. As shown in Fig. 3d, the tumor tissue will possess the enhanced CT imaging signal after the intratumoral injection of $\text{BiVO}_4/\text{Fe}_3\text{O}_4$ @PDA SPs. In contrast, only normal bone structures can be observed without the injection of $\text{BiVO}_4/\text{Fe}_3\text{O}_4$ @PDA SPs. Meanwhile, the mouse treated by $\text{BiVO}_4/\text{Fe}_3\text{O}_4$ @PDA SPs displays a clear T₂-weighted MR imaging in the tumor region comparing to the region without the SP injection (Fig. 3e). As for PA imaging, the PA signal of tumor is notably enhanced after intratumoral injection of $\text{BiVO}_4/\text{Fe}_3\text{O}_4$ @PDA SPs. As a comparison, only extremely weak PA signal arising from the tumor

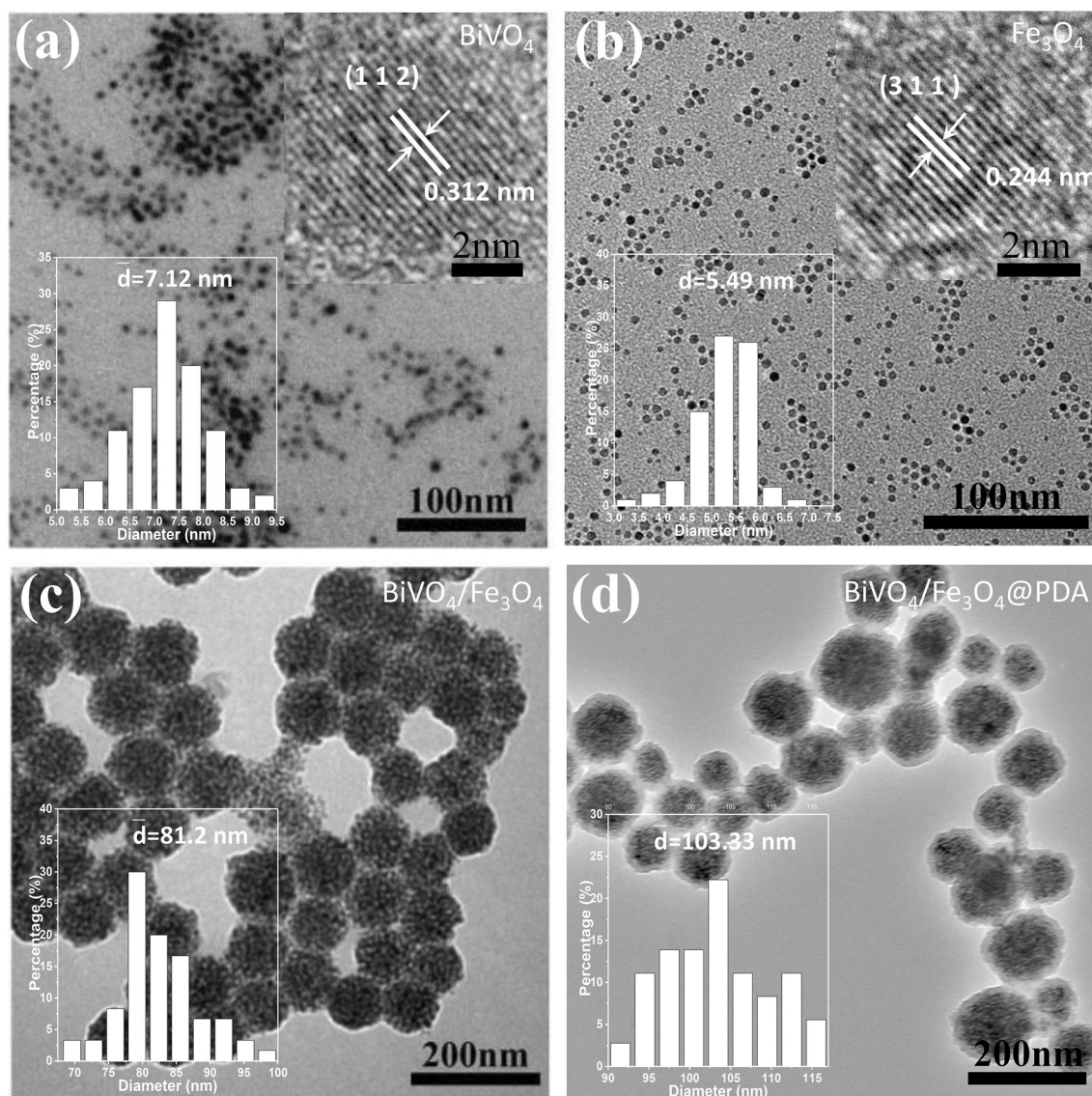


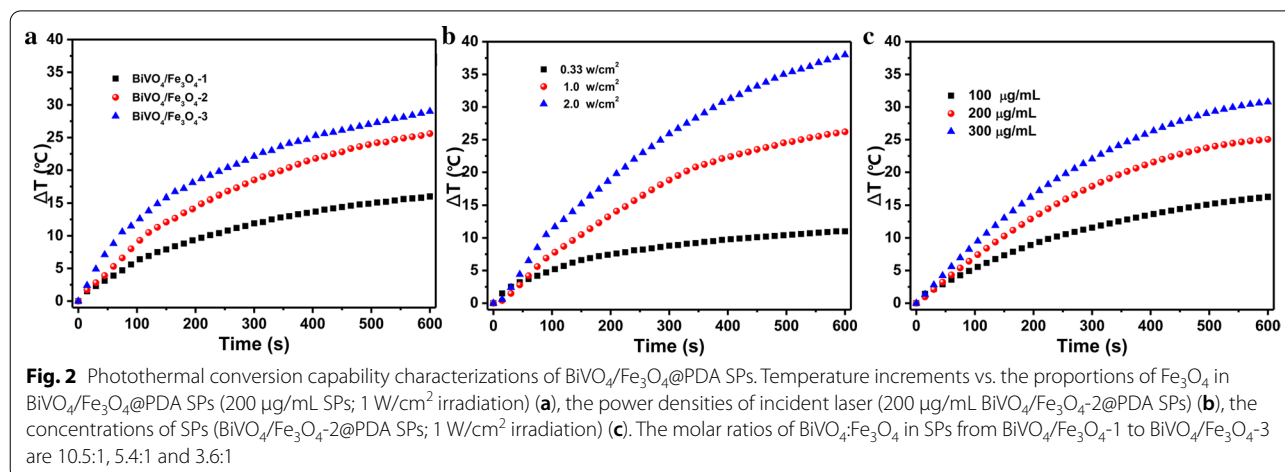
Fig. 1 TEM and HRTEM characterizations of BiVO_4 NPs, Fe_3O_4 NPs, $\text{BiVO}_4/\text{Fe}_3\text{O}_4$ SPs and $\text{BiVO}_4/\text{Fe}_3\text{O}_4@PDA$ SPs. TEM images of (a) BiVO_4 NPs, (b) Fe_3O_4 NPs, (c) $\text{BiVO}_4/\text{Fe}_3\text{O}_4$ SPs and (d) $\text{BiVO}_4/\text{Fe}_3\text{O}_4@PDA$ SPs. Inset in (a) and (b): size distributions and HRTEM images of BiVO_4 and Fe_3O_4 NPs. Inset in (c) and (d): size distributions of $\text{BiVO}_4/\text{Fe}_3\text{O}_4$ SPs and $\text{BiVO}_4/\text{Fe}_3\text{O}_4@PDA$ SPs

blood can be detected in the tumor site without the injection of $\text{BiVO}_4/\text{Fe}_3\text{O}_4@PDA$ SPs (Fig. 3f). The results above suggest the great potentials of $\text{BiVO}_4/\text{Fe}_3\text{O}_4@PDA$ SPs in multimodal imaging, which could combine advantages of each technique to provide complementary information for accurate diagnosis.

Thereafter, the *in vitro* synergistic therapeutic effects of $\text{BiVO}_4/\text{Fe}_3\text{O}_4@PDA$ SPs are evaluated via clonogenic assay (Fig. 4a and b). KB cells are treated by X-rays with different radiation doses (2 to 8 Gy) or NIR laser (0.33 W cm^{-2}) in the absence or presence of SPs (100 $\mu\text{g/mL}$). The result manifests that NIR alone and X-ray

alone treatments can decrease the colony formation of KB cells to 88.2% and 61.3%, whereas SPs + NIR and SPs + X-ray can inhibit cell survival to 10.1% and 12.0%. Surprisingly, only 2.1% cells survive after the treatment of SPs + X-ray + NIR. Moreover, compared to the colony forming efficiency under X-ray treatment alone, the same therapeutic effect can be achieved under lower X-ray dose in the X-ray + NIR group, which strongly certify the considerable synergistic therapeutic efficacy between RT and PTT (Fig. 4c).

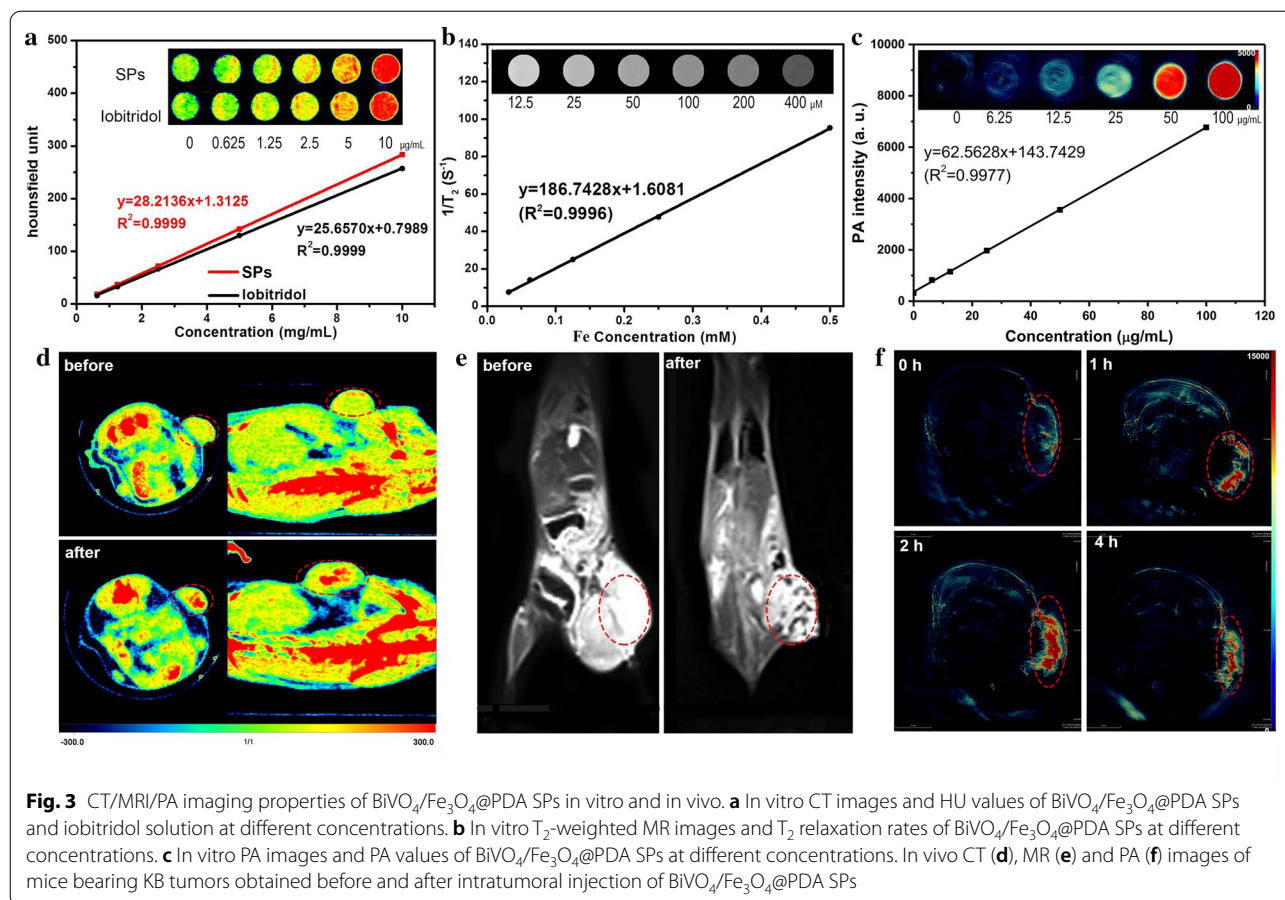
Next, 2',7'-dichlorodihydrofluorescein diacetate (DCFH-DA) fluorescent probe is employed to detect



intracellular oxidative stress level of KB cells after different treatments [38]. As shown in Fig. 4d, there is no detectable fluorescence in cells treated by PBS, SPs, NIR or SPs + NIR. In contrast, cells under X-ray, SPs + X-ray, SPs + NIR + X-ray treatments exhibit the bright fluorescence, and their fluorescence intensities are gradually enhanced. Since high radiation energy deposition and enhanced oxidative stress may facilitate the damage of DNA, γ -H2AX staining is performed to analyze the damage of DNA double-strand in cell nuclei quantitatively (Fig. 4e) [39]. As similar as the ROS assay, no visible fluorescence is found in cells without the X-ray treatment. The apparent fluorescence can be seen in cells under the treatments of X-ray, SPs + X-ray and SPs + NIR + X-ray, and the SPs + NIR + X-ray treatment produce the highest fluorescence intensity. Both DCFH-DA and γ -H2AX assays demonstrate the synergistic therapeutic efficacy of RT and PTT.

Motivated by the effective in vitro therapeutic outcome, the subcutaneous tumor model is employed to investigate the antitumor efficacy of $\text{BiVO}_4/\text{Fe}_3\text{O}_4$ @PDA SPs in vivo. The KB tumor-bearing BALB/c nude mice are randomly divided into 7 groups according to various treatments: (1) PBS, (2) SPs, (3) NIR, (4) X-rays, (5) SPs + NIR, (6) SPs + X-rays, (7) SPs + NIR + X-rays. Mice in group (3), (5) and (7) are irradiated by an 808 nm laser (0.33 W/cm^2) for 10 min after the injection of $\text{BiVO}_4/\text{Fe}_3\text{O}_4$ @PDA SPs. Additional file 1: Figure S9 exhibits the IR thermographs of mice at different time intervals. The temperature of tumor tissue treated by SPs exhibits a rapid increase of 19°C within 10 min, which is sufficient for tumor ablation. In contrast, there is no significant temperature elevation in the tumor without SPs injection. This dramatic difference lead to the remarkable localized overheat at the tumor site under NIR irradiation, causing severe tumor damage without influencing the adjacent

normal tissues. Tumor volumes within 16 days in each group are recorded (Fig. 5a). The tumor volumes in group (1), (2) and (3) increase rapidly, suggesting the negligible effect of SPs alone and NIR alone treatments on the inhibition of tumor growth. Tumors in group (4) grow slowly comparing with those in group (1), revealing the irradiation of X-ray can only inhibit the tumor growth mildly. Despite SPs + X-ray and SPs + NIR treatments have the significantly inhibition on the growth of tumor at the initial stage of treatment, there are recurrences can be found after the treatment for about 10 days. Surprisingly, nearly complete tumor inhibition is realized in group (7) in the absence of recurrence. The weights and photographs of tumors exhibited in Fig. 5b and c further verifies that the synergistic therapeutic efficacy of RT and PTT are better than any single treatment. Because the weights of mice in each group are steady without distinct fluctuation, the side-effects of all the treatments during the therapeutic process can be excluded (Fig. 5e). According to the hematoxylin and eosin (H&E) staining images of tumor tissues (Fig. 5g), the death and nucleus rupture and ablation of cancer cells can be observed in tumors under SPs + X-ray and SPs + NIR treatments, whereas the tumors in group (7) have the most serious cell damage. This result further demonstrates the combination of RT with PTT can greatly improve the therapeutic effect compared to any single treatment. Besides the overlap of RT and PTT, the excellent synergistic therapeutic efficacy of $\text{BiVO}_4/\text{Fe}_3\text{O}_4$ @PDA SPs on tumor inhibition may come from the alleviation of hypoxia status in tumor tissues by boosting intratumoral blood circulation under NIR irradiation. Additional file 1: Figure S10 shows the in vivo PA images of tumors under various treatments: (1) PBS, (2) NIR, (3) SPs, (4) SPs + NIR, which imply that the photothermal conversion capability of $\text{BiVO}_4/\text{Fe}_3\text{O}_4$ @PDA SPs can



remarkably increase tumor oxygenation, making tumor cells more sensitive to RT.

At last, the biosafety profile of $\text{BiVO}_4/\text{Fe}_3\text{O}_4$ @PDA SPs is evaluated by using BALB/c nude mice. H&E staining assays of major organs show that different treatments have no significant effects in the organ tissues of heart, liver, spleen, lung and kidney (Additional file 1: Figure S11). Serum biochemistry analysis exhibits the negligible side-effects on blood glucose and lipid, liver and renal function tests after the injection of SPs and combined treatments (Additional file 1: Figure S12). All these results mentioned above testify the excellent biocompatibility and powerful lethality of $\text{BiVO}_4/\text{Fe}_3\text{O}_4$ @PDA SPs.

Conclusions

In summary, we demonstrate on the design and preparation of $\text{BiVO}_4/\text{Fe}_3\text{O}_4$ @PDA SPs by using BiVO_4 and Fe_3O_4 NPs as the building blocks. BiVO_4 NPs endow $\text{BiVO}_4/\text{Fe}_3\text{O}_4$ @PDA SPs with impressive X-ray absorption capability due to the high X-ray attenuation coefficient of Bi, which is benefit for their utilization as radiosensitizers for CT imaging and RT. On the other hand, the

superparamagnetic of Fe_3O_4 NPs strongly guarantee the application of $\text{BiVO}_4/\text{Fe}_3\text{O}_4$ @PDA SPs as T_2 -weighted contrast agent for MR imaging. Furthermore, the aggregation of Fe_3O_4 NPs in SPs and the presence of PDA shell greatly improve the photothermal conversion capability of SPs, making $\text{BiVO}_4/\text{Fe}_3\text{O}_4$ @PDA SPs as an ideal photothermal transducer for PA imaging and PTT. By integrating the advantages of various imaging modalities (CT/PA/MR) and therapeutic strategies (RT/PTT), our $\text{BiVO}_4/\text{Fe}_3\text{O}_4$ @PDA SPs exhibit the sensitive multi-modal imaging capability and superior synergistic therapeutic efficacy for tumors. Since there are many kinds of building blocks with unique properties appropriating for self-assembly, our work may largely enrich the library of nanomaterials for tumor theranostic.

Methods

Materials

$\text{Bi}(\text{NO}_3)_3 \cdot 5\text{H}_2\text{O}$ (99.0%, Aladdin), NH_4VO_3 (99.9%, Aladdin), $\text{Fe}(\text{acac})_3$ (99.9%, Simga-Aldrich), oleyamine (OLA, 70%, Simga-Aldrich), 1,2-hexadecanediol (90%, Aladdin), oleic acid (OA, 90%, Simga-Aldrich), SDS (99%, Simga-Aldrich), 1-octadecene (ODE, 90%, Simga-Aldrich),

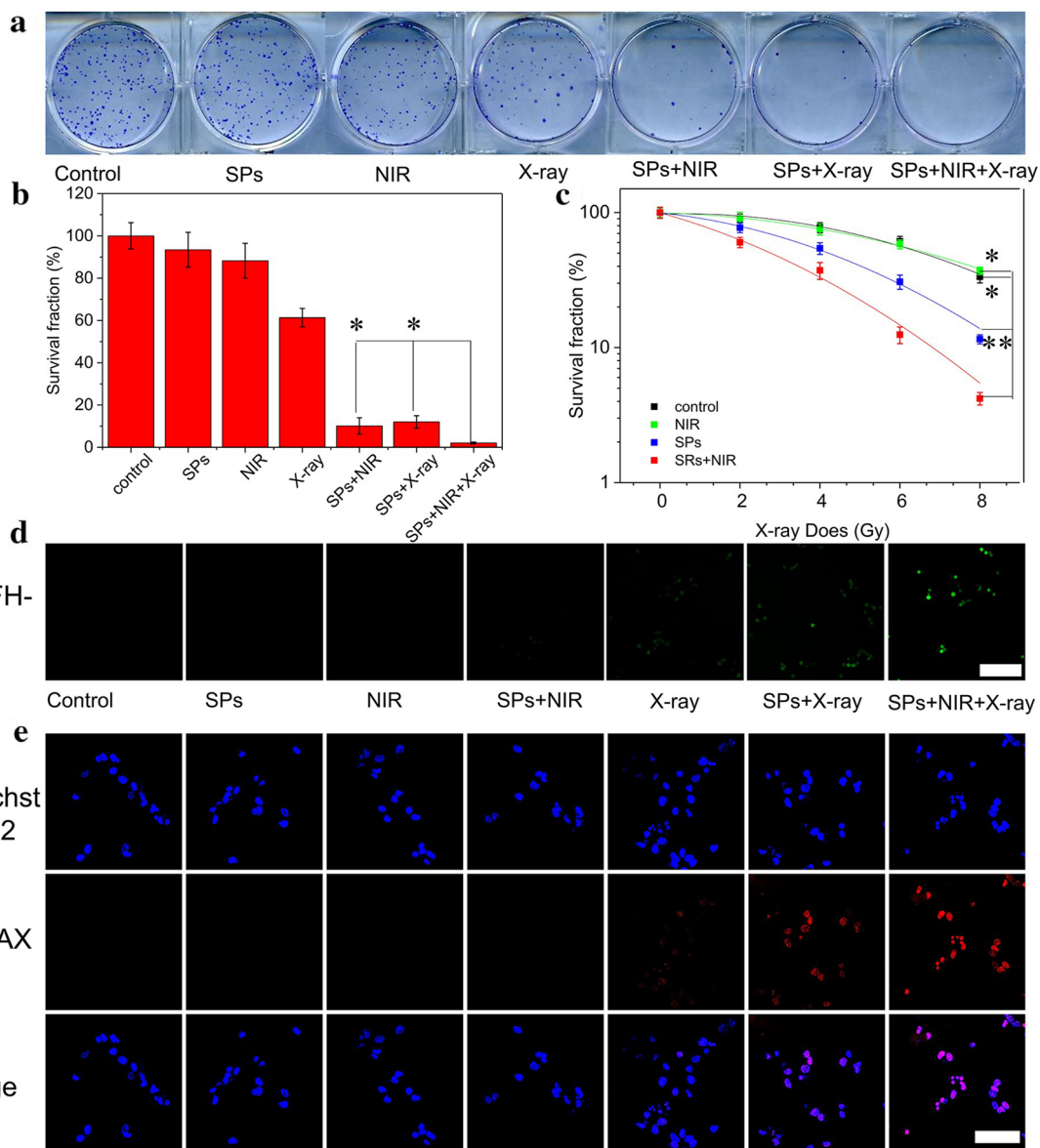
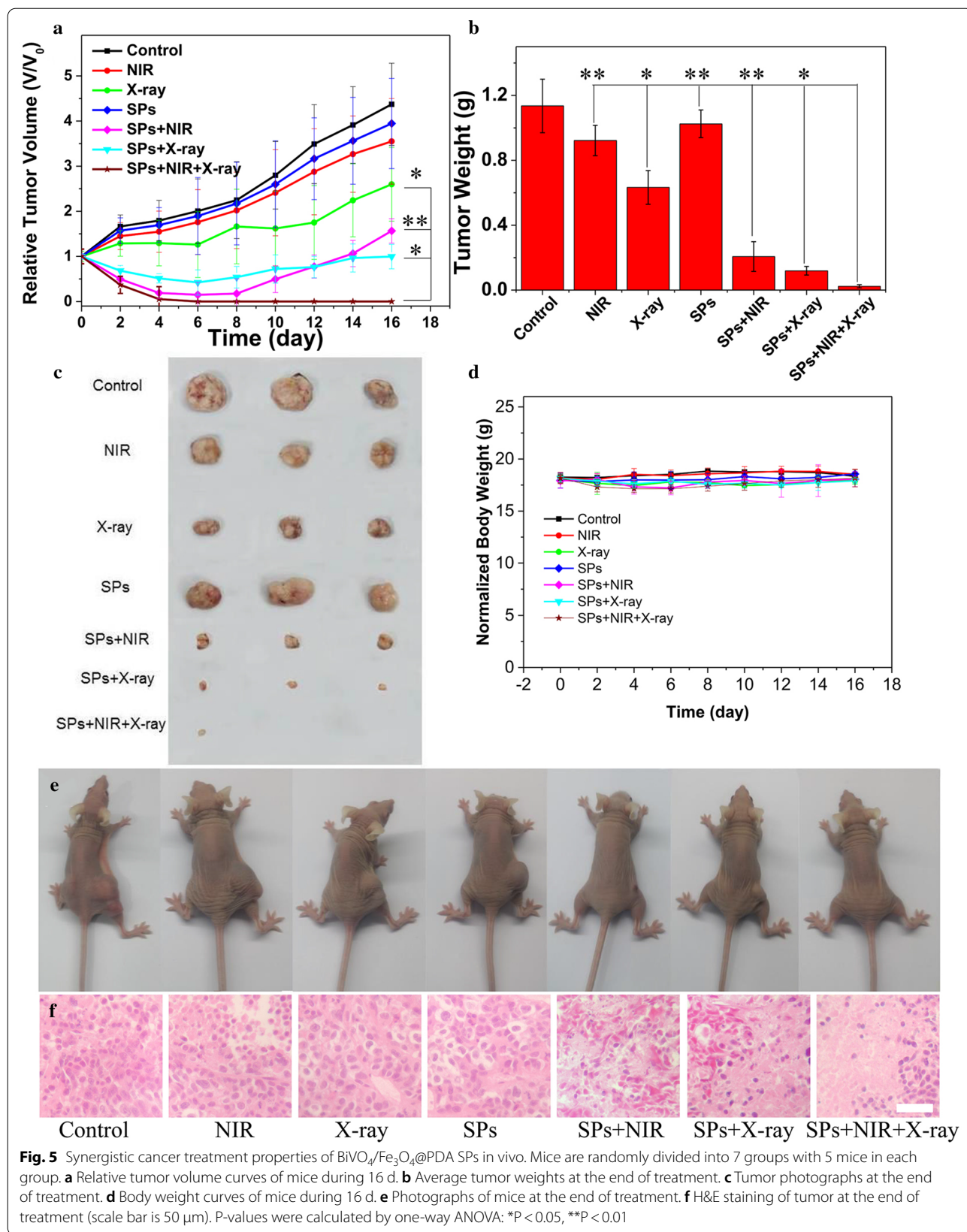


Fig. 4 Synergistic cancer treatment properties of $\text{BiVO}_4/\text{Fe}_3\text{O}_4/\text{PDA}$ SPs in vitro. **a** Clonogenic assay of KB cells under different treatments (NIR: 0.33 W/cm^2 and 10 min; X-ray: 6 Gy). **b** Survival fraction of KB cells under different treatments (NIR: 0.33 W/cm^2 and 10 min; X-ray: 6 Gy). **c** Survival fraction of KB cells under different treatments and X-ray dose. **d** ROS production in KB cells under different treatments (scale bar is $200 \mu\text{m}$). **e** $\gamma\text{-H2AX}$ staining in KB cells under different treatments (scale bar is $40 \mu\text{m}$). P-values were calculated by one-way ANOVA: * $P < 0.05$, ** $P < 0.01$

tris(hydroxymethyl) aminomethans (Tris, >99%, Aladdin), DA (99.0%). $\gamma\text{-H2AX}$ (phospho S139) antibody [EP854(2)Y] (Alexa Fluor 568) (ab206901) was purchased from Abcam. Crystal violet staining solution, CCK-8, hoechst 33,342 and ROS assay kit were purchased from Beyotime.

Preparation of BiVO_4 NPs

1 mmol $\text{Bi}(\text{NO}_3)_3 \cdot 5\text{H}_2\text{O}$, 2 mL OLA, 2 mL OA and 10 mL ODE were added into a 100 mL three-necked flask. The temperature was raised to $175 \text{ }^\circ\text{C}$ in nitrogen atmosphere under vigorous stirring. When the solution was completely clear, the solution was dropped to $130 \text{ }^\circ\text{C}$, followed by the addition of 10 mL water containing 2 mmol NH_4VO_3 . The resulting solution was heated at $100 \text{ }^\circ\text{C}$ for 5 min and cooled down to room temperature naturally.



After that, the solution was uniformly mixed with ethanol, and the bottom aqueous layer of the mixture was discarded. The upper organic layer was mixed with water and ethanol for twice, and the bottom aqueous layer of the mixture was discarded. The final product was washed by ethanol for another three times and dispersed in toluene.

Preparation of Fe₃O₄ NPs

OA-capped Fe₃O₄ NPs were prepared by the thermal decomposition route. 2 mmol Fe(acac)₃, 2 mL OA, 2 mL OLA, 5 mmol 1,2-hexadecanediol and 20 mL benzyl ether were added into a 100 mL three-necked flask. The mixture was heated at 200 °C for 30 min under nitrogen atmosphere, followed by reflux at 265 °C for 30 min. After that, the solution was dropped to room temperature naturally, and the product was washed for three times by ethanol and finally dispersed in toluene.

Preparation of SDS-capped BiVO₄/Fe₃O₄ SPs

2 mL toluene containing 50 mg BiVO₄ NPs and 20 mg Fe₃O₄ NPs was added into 5 mL aqueous solution containing 10 mg SDS. After ultrasonic stirring for 10 min, the resulting emulsions were heated at 60 °C for another 30 min to evaporate toluene. After that, solution was centrifuge at 3000 r/min for 5 min, and the SDS-capped BiVO₄/Fe₃O₄ SPs were obtained.

Preparation of BiVO₄/Fe₃O₄@PDA SPs

DA monomer was added into 10 mL Tris-buffer solution (10 mM, pH 8.5) containing 5 mg SDS-capped BiVO₄/Fe₃O₄ SPs. After stirring for 3 h, the reaction solution was centrifuged at 5000 r/min for 30 min. Then, BiVO₄/Fe₃O₄@PDA SPs were obtained.

Characterization

TEM was taken on a Hitachi H-800 electron microscope (200 kV) coupled with a CCD camera. UV-vis absorption spectra were obtained using a Lambda 800 UV-vis spectrophotometer. HRTEM and EDS were performed on a JEM-2100F electron microscope at an acceleration voltage of 200 kV with an EDS detector. XRD was implemented on an Empyrean X-ray diffractometer with Cu K radiation ($\lambda = 1.5418 \text{ \AA}$).

Cell experiment

Cytotoxicity assay

We used CCK-8 and KB cells to test the cytotoxicity of SPs. In the 96-well plate, we cultured 5000 cells for each well. The cells were incubated at 37 °C with 5% CO₂ for 24 h. Then the cells were treated with different concentrations of SPs and further incubated for 24 h. After that, the medium was removed and the cells were washed

twice with PBS. Solarbio 1640 medium is re-added with 10 μL of CCK-8 and the cells were continued to culture for 1 h. Finally, the microplate reader was used to measure the absorbance at 450 nm.

Clonogenic assay

In the 6-well plate, we cultured 1000 KB cells for each well. After co-cultivation with SPs (100 $\mu\text{g}/\text{mL}$) overnight, the cells were first treated with NIR (0.33 W/cm², 10 min), then X-rays (0, 2, 4, 6, 8 Gy) sequentially. After that, the cells were washed with PBS and continued to incubate for 10 days. Finally, the cells were stained with crystal violet staining solution. Surviving fraction (SF) was calculated by (surviving colonies)/(cells seeded \times plating efficiency). The mean surviving fraction was obtained from three parallel samples. The SF and the radiation dose can be fitted using the following formula: $SF = \exp[-(\alpha D + \beta D^2)]$

ROS in cells

We use ROS assay kit to detect ROS in cells. In the 6-well plate, we cultured 50,000 KB cells in each well. We used SPs (100 $\mu\text{g}/\text{mL}$) to co-cultivate with cells overnight, followed by washing the cells with PBS for three times. We added the 1000-fold diluted ROS assay kit to each well and washed the cells with PBS for three times after incubation for 20 min. Then we treated the cells with X-ray (6 Gy) or NIR (0.33 W/cm², 10 min). The cells were first irradiated by NIR, then by X-ray. Finally, the cells were observed using the FV1000 laser scanning confocal microscopy (excitation wavelength: 488 nm; emission wavelength: 525 nm).

DNA double-strand breaks

In the 6-well plate, we cultured 50,000 KB cells in each well. We used SPs (100 $\mu\text{g}/\text{mL}$) to co-cultivate with cells overnight, followed by treatment of cells with X-ray (6 Gy) or NIR (0.33 W/cm², 10 min). The cells were first irradiated by NIR, then by X-ray. We fixed the cells with paraformaldehyde (4%) for 10 min and washed with PBS for three times. It was then permeabilized with methanol and washed with PBS for three times. The cells were exposed in blocking buffer for 1 h and further incubated with 100-fold $\gamma\text{-H2AX}$ (phospho S139) antibody [EP854(2)Y] (Alexa Fluor 568) (ab206901) at 4 °C overnight and then washed with PBS for three times (excitation wavelength: 578 nm; emission wavelength: 603 nm). The cells were stained with Hoechst 33,342 (excitation wavelength: 350 nm; emission wavelength: 461 nm) and washed with PBS for three times. Finally, the cells were observed using FV1000 laser scanning confocal microscopy.

Animal experiment

In vivo RT/PTT synergistic treatment

KB cells were subcutaneously injected into the right leg of BALB/c nude mice. When the average tumor volume reached 75 mm^2 , mice were randomly divided into 7 groups with 5 mice in each group according to different treatment conditions: (1) PBS, (2) SPs, (3) NIR, (4) X-rays, (5) SPs + NIR, (6) SPs + X-rays, (7) SPs + NIR + X-rays. We injected $20 \mu\text{L}$ of SPs (5 mg/mL) into the tumor via intratumoral injection. Mice in the corresponding groups were then treated with NIR (0.33 W/cm^2 , 10 min) or X-ray (6 Gy). Tumor volumes and body weights of mice in each group were recorded after this treatment. Finally, all the mice were sacrificed and the blood, heart, liver, spleen, lung, kidney and tumor were taken. The blood was centrifuged and the serum was taken for the blood analysis. The tumors and other organs were weighed and used for H&E staining.

CT imaging

In vivo and *in vitro* CT imaging were used U-SPECT+/CT (MILABS). For *in vitro* imaging, we prepared aqueous solutions of different concentrations of SPs and iopromide and measured their HU values. For *in vivo* imaging, BALB/c nude mice harboring KB tumors were intratumoral injected with $50 \mu\text{L}$, 10 mg/mL SPs solution.

MR imaging

We used SIEMENS Avanto 1.5T clinical MRI unit to assess the MR imaging property of SPs. For *in vitro* imaging, we prepared aqueous solutions of different concentrations of SPs for measuring. For *in vivo* imaging, BALB/c nude mice with KB tumors were intratumoral injected with $20 \mu\text{L}$, 10 mg/mL SPs solution.

PA imaging

In vivo and *in vitro* PA imaging was used MSOT INVI-SIO-256 (iThera Medical). For *in vitro* imaging, we prepared aqueous solutions of different concentrations of SPs for measuring. For *in vivo* imaging, BALB/c nude mice with KB tumors were intratumoral injected with $20 \mu\text{L}$, 10 mg/mL SPs solution.

Supplementary Information

The online version contains supplementary material available at <https://doi.org/10.1186/s12951-021-00802-x>.

Additional file 1: Figure S1. XRD patterns of BiVO_4 and Fe_3O_4 NPs. **Figure S2.** EDS-Mapping images of the $\text{BiVO}_4/\text{Fe}_3\text{O}_4$ SPs. **Figure S3.** TEM images of $\text{BiVO}_4/\text{Fe}_3\text{O}_4$ @PDA SPs with different sizes. **Figure S4.** TEM images of $\text{BiVO}_4/\text{Fe}_3\text{O}_4$ @PDA SPs with different thicknesses of the PDA shell. **Figure S5.** UV-vis absorption spectra of BiVO_4 NPs, Fe_3O_4 NPs, $\text{BiVO}_4/\text{Fe}_3\text{O}_4$ SPs and $\text{BiVO}_4/\text{Fe}_3\text{O}_4$ @PDA SPs. **Figure S6.** Photothermal conversion efficiency calculation of $\text{BiVO}_4/\text{Fe}_3\text{O}_4$ @PDA SPs. **Figure S7.** Concentration-related cytotoxicity of $\text{BiVO}_4/\text{Fe}_3\text{O}_4$ @PDA SPs. **Figure S8.** Colloidal stability of

$\text{BiVO}_4/\text{Fe}_3\text{O}_4$ @PDA SPs. **Figure S9.** Infrared imaging photographs of KB tumor-bearing mice with or without SPs injection. **Figure S10.** PA imaging of tumor oxygenation of tumors under the treatments. **Figure S11.** H&E stained photographs of organs after treatment. **Figure S12.** Blood biochemistry analyses of mice after different treatments. **Table S1.** $\text{BiVO}_4/\text{Fe}_3\text{O}_4$ SPs with different Bi/Fe element ratios.

Authors' contributions

ZW designed and carried out experiments and wrote the manuscript. TTK synthesized the $\text{BiVO}_4/\text{Fe}_3\text{O}_4$ @Polydopamine superparticles with supervision from HYZ and YL. GW obtained and analyzed data. SWL and LW completed most of the *in vivo* and *in vitro* experiments. HYZ, YC and YL proposed and supervised the project. All authors read and approved the final manuscript.

Funding

This work was supported by NSFC (No. 21875086, 21906110), JLU Science and Technology Innovative Research Team (2017TD-06), Y.C. appreciates the support from the Natural Science Foundation of Jiangsu Province (BK20170353).

Availability of data and materials

All sequence data generated and analysed during the current study are available in the NCBI database under the project accession number PRJNA597946, (<https://www.ncbi.nlm.nih.gov/sra/PRJNA597946>).

Ethics approval and consent to participate

Not applicable.

Consent for publication

Not applicable.

Competing interests

The authors declare that they have no competing interests.

Author details

¹ State Key Laboratory of Supramolecular Structure and Materials, Jilin University, Changchun 130012, People's Republic of China. ² Key Laboratory of Polymer Ecomaterials, Changchun Institute of Applied Chemistry, Chinese Academy of Sciences, Changchun 130012, People's Republic of China. ³ State Key Laboratory of Radiation Medicine and Protection, School for Radiological and Interdisciplinary Sciences (RAD-X), Collaborative Innovation Center of Radiation Medicine of Jiangsu Higher Education Institutions, Soochow University, Suzhou 215123, People's Republic of China. ⁴ Department of Gastroenterology, China-Japan Union Hospital, Jilin University, Changchun 130033, People's Republic of China. ⁵ Department of Oral Pathology, School and Hospital of Stomatology, Jilin University, Changchun 130021, People's Republic of China.

Received: 10 October 2020 Accepted: 9 February 2021

Published online: 29 March 2021

References

- Bernier J, Hall EJ, Giaccia A. Radiation oncology: a century of achievements. *Nat Rev Cancer*. 2004;4:737–47.
- Baumann M, Krause M, Hill R. Exploring the role of cancer stem cells in radioresistance. *Nat Rev Cancer*. 2008;8:545–54.
- Zappa C, Mousa SA. Non-small cell lung cancer: current treatment and future advances. *Transl Lung Cancer R*. 2016;5:288–300.
- Weichselbaum RR, Liang H, Deng L, Fu Y. Radiotherapy and immunotherapy: a beneficial liaison? *Nat Rev Clin Oncol*. 2017;14:365–79.
- Atun R, Jaffray DA, Barton MB, Bray F, Baumann M, Vikram B, Hanna TP, Knaut FM, Lievens Y, Lui TYM, Milosevic M, O'Sullivan B, Rodin DL, Rosenblatt E, Van DJ, Yap ML, Zubizarreta E, Gospodarowicz M. Expanding global access to radiotherapy. *Lancet Oncol*. 2015;16:1153–86.
- Prasad P, Gordijo CR, Abbasi AZ, Maeda A, Ip A, Rauth AM, DaCosta RS, Wu XY. Multifunctional albumin– MnO_2 nanoparticles modulate solid tumor microenvironment by attenuating hypoxia, acidosis, vascular

- endothelial growth factor and enhance radiation response. *ACS Nano*. 2014;8:3202–12.
7. Antosh MP, Wijesinghe DD, Shrestha S, Lanou R, Huang YH, Hasselbacher T, Fox D, Neretti N, Sun S, Katenka N, Cooper LN, Andreev OA, Reshetnyak YK. Enhancement of radiation effect on cancer cells by gold-pHLIP. *Proc Natl Acad Sci*. 2015;112:5372–6.
 8. Dufort S, Bianchi A, Henry M, Lux F, Duc GL, Josserand V, Louis C, Perriat P, Crémillieux Y, Tillement O, Coll JL. Nebulized gadolinium-based nanoparticles: a theranostic approach for lung tumor imaging and radiosensitization. *Small*. 2015;11:215–21.
 9. Wang H, Zeng ZC, Bui TA, DiBiase SJ, Qin W, Xia F, Powell SN, Iliakis G. Replication protein A2 phosphorylation after DNA damage by the coordinated action of ataxia telangiectasia-mutated and DNA-dependent protein kinase. *Cancer Res*. 2001;61:8554–63.
 10. Liu Y, Ai K, Lu L. Nanoparticulate X-ray computed tomography contrast agents: from design validation to in vivo applications. *Acc Chem Res*. 2012;45:1817–27.
 11. Lei P, Zhang P, Yuan Q, Wang Z, Dong L, Song S, Xu X, Liu X, Feng J, Zhang H. $\text{Yb}^{3+}/\text{Er}^{3+}$ -codoped Bi_2O_3 nanospheres: probe for upconversion luminescence imaging and binary contrast agent for computed tomography imaging. *ACS Appl Mater Interfaces*. 2015;7:26346–54.
 12. Dong X, Cheng R, Zhu S, Liu H, Zhou R, Zhang C, Chen K, Mei L, Wang C, Su C, Liu X, Gu Z, Zhao Y. A heterojunction structured WO_3/WSe_2 nanoradiosensitizer increases local tumor ablation and checkpoint blockade immunotherapy upon low radiation dose. *ACS Nano*. 2020;14:5400–16.
 13. Feng L, Dong Z, Liang C, Chen M, Tao D, Cheng L, Yang K, Liu Z. Iridium nanocrystals encapsulated liposomes as near-infrared light controllable nanozymes for enhanced cancer radiotherapy. *Biomaterials*. 2018;181:81–91.
 14. Gong F, Chen J, Han X, Zhao J, Wang M, Feng L, Li Y, Liu Z, Cheng L. Core-shell $\text{TaO}_x/\text{MnO}_2$ nanoparticles as a nano-radiosensitizer for effective cancer radiotherapy. *J Mater Chem B*. 2018;6:2250–57.
 15. Chen R, Liu H, Dong X, Zhu S, Zhou R, Wang C, Wang Y, Wang X, Su C, Gu Z. Semiconductor heterojunction-based radiocatalytic platforms for tumors treatment by enhancing radiation response and reducing radioresistance. *Chem Eng J*. 2020;394:124827.
 16. Sahu A, Kwon I, Tae G. Improving cancer therapy through the nanomaterials-assisted alleviation of hypoxia. *Biomaterials*. 2020;228:119578.
 17. Cheng Y, Kong X, Chang Y, Feng Y, Zheng R, Wu X, Xu K, Gao X, Zhang H. Spatiotemporally synchronous oxygen self-supply and reactive oxygen species production on Z-scheme heterostructures for hypoxic tumor therapy. *Adv Mater*. 2020;32:1908109.
 18. Horsman MR, Overgaard J. Hyperthermia: a potent enhancer of radiotherapy. *Clin Oncol*. 2007;19:418–26.
 19. Shen S, Chao Y, Dong Z, Wang G, Yi X, Song G, Yang K, Liu Z, Cheng L. Bottom-up preparation of uniform ultrathin rhenium disulfide nanosheets for image-guided photothermal radiotherapy. *Adv Funct Mater*. 2017;27:1700250.
 20. Wang S, Li X, Chen Y, Cai X, Yao H, Gao W, Zheng Y, An X, Shi J, Chen H. A facile one-pot synthesis of a two-dimensional $\text{MoS}_2/\text{Bi}_2\text{S}_3$ composite theranostic nanosystem for multi-modality tumor imaging and therapy. *Adv Mater*. 2015;27:2775–82.
 21. Zhou J, Li M, Hou Y, Luo Z, Chen Q, Cao H, Huo R, Xue C, Sutrisno L, Hao L, Cao Y, Ran H, Lu L, Li K, Cai K. Engineering of a nanosized biocatalyst for combined tumor starvation and low-temperature photothermal therapy. *ACS Nano*. 2018;12:2858–72.
 22. Schwenzer NF, Springer F, Schraml C, Stefan N, Machann J, Schick F. Non-invasive assessment and quantification of liver steatosis by ultrasound, computed tomography and magnetic resonance. *J Hepatol*. 2009;51:433–45.
 23. Smith BR, Gambhir SS. Nanomaterials for in vivo imaging. *Chem Rev*. 2017;117:901–86.
 24. Yip SSF, Aerts HJWL. Applications and limitations of radiomics. *Phys Med Biol*. 2016;61:R150–66.
 25. Iima M, Bihan DL. Clinical intravoxel incoherent motion and diffusion MR imaging: past, present, and future. *Radiology*. 2016;278:13–32.
 26. Fu QR, Zhu R, Song JB, Yang HH, Chen XY. Photoacoustic imaging: contrast agents and their biomedical applications. *Adv Mater*. 2019;31:1805875.
 27. Hu X, Sun J, Li F, Li R, Wu J, He J, Wang N, Liu J, Wang S, Zhou F, Sun X, Kim D, Hyeon T, Ling D. Renal-clearable hollow bismuth subcarbonate nanotubes for tumor targeted computed tomography imaging and chemoradiotherapy. *Nano Lett*. 2018;18:1196–204.
 28. Wang X, Zhang C, Du J, Dong X, Jian S, Yan L, Gu Z, Zhao Y. Enhanced generation of non-oxygen dependent free radicals by Schottky-type heterostructures of $\text{Au-Bi}_2\text{S}_3$ nanoparticles via X-ray-induced catalytic reaction for radiosensitization. *ACS Nano*. 2019;13:5947–58.
 29. Wang X, Guo Z, Zhang C, Zhu S, Li L, Gu Z, Zhao Y. Ultrasmall BiOI quantum dots with efficient renal clearance for enhanced radiotherapy of cancer. *Adv Sci*. 2020;7:1902561.
 30. Wang Y, Guo Q, Su G, Cao J, Liu J, Zhang X. Hierarchically structured self-healing actuators with superfast light- and magnetic-response. *Adv Funct Mater*. 2019;29:1906198.
 31. Chen O, Riedemann L, Etoc F, Herrmann H, Coppey M, Barch M, Farrar CT, Zhao J, Bruns OT, Wei H, Guo P, Cui J, Jensen R, Chen Y, Harris DK, Cordero JM, Wang Z, Jasanoff A, Fukumura D, Reimer R, Dahan M, Jain RK, Bawendi MG. Magneto-fluorescent core-shell supernanoparticles. *Nat Commun*. 2014;5:5093.
 32. He J, Huang X, Li YC, Liu Y, Babu T, Aronova MA, Wang S, Lu Z, Chen X, Nie Z. Self-assembly of amphiphilic plasmonic micelle-like nanoparticles in selective solvents. *J Am Chem Soc*. 2013;135:7974–84.
 33. Xia Y, Tang Z. Monodisperse inorganic supraparticles: formation mechanism, properties and applications. *Chem Commun*. 2012;48:6320–36.
 34. Dong C, Lu S, Yao S, Ge R, Wang Z, Wang Z, An P, Liu Y, Yang B, Zhang H. Colloidal synthesis of ultrathin monoclinic BiVO_4 nanosheets for Z-scheme overall water splitting under visible light. *ACS Catal*. 2018;8:8649–58.
 35. Sun S, Zeng H. Size-controlled synthesis of magnetite nanoparticles. *J Am Chem Soc*. 2002;124:8204–5.
 36. Zhuang J, Wu H, Yang Y, Cao YC. Controlling colloidal superparticle growth through solvophobic interactions. *Angew Chem Int Ed*. 2008;47:2208–12.
 37. Tang L, Yang X, Yin Q, Cai K, Wang H, Chaudhury I, Yao C, Zhou Q, Kwon M, Hartman JA, Dobrucki IT, Dobrucki LW, Borst LB, Lezmi S, Helferich WG, Ferguson AL, Fan TM, Cheng J. Investigating the optimal size of anticancer nanomedicine. *Proc Natl Acad Sci*. 2014;111:15344–9.
 38. Zhu Y, Li W, Zhang Y, Li J, Liang L, Zhang X, Chen N, Sun Y, Chen W, Tai R, Fan C, Huang Q. Excessive sodium ions delivered into cells by nanodiamonds: implications for tumor therapy. *Small*. 2012;8:1771–9.
 39. Srinivas US, Tan BWQ, Vellayappan BA, Jayasekharan AD. ROS and the DNA damage response in cancer. *Redox Biol*. 2019;25:101084.

Publisher's note

Springer Nature remains neutral with regard to jurisdictional claims in published maps and institutional affiliations.

Ready to submit your research? Choose BMC and benefit from:

- fast, convenient online submission
- thorough peer review by experienced researchers in your field
- rapid publication on acceptance
- support for research data, including large and complex data types
- gold Open Access which fosters wider collaboration and increased citations
- maximum visibility for your research: over 100M website views per year

At BMC, research is always in progress.

Learn more biomedcentral.com/submissions

